

# Using finite volume method for investigating the turbulent flow field and heat transfer of a non-Newtonian nanofluid in a channel with triangular vortex generators

Muhammad Ibrahim (✉ [mibrahim@amss.ac.cn](mailto:mibrahim@amss.ac.cn))

University of Science and Technology

Tareq Saeed

King Abdulaziz University

---

## Research Article

**Keywords:** non-Newtonian nanofluid, Triangular Vortex Generator, Turbulent Flow, SIMPLE Algorithm, Mean Nusselt number,

**Posted Date:** March 16th, 2021

**DOI:** <https://doi.org/10.21203/rs.3.rs-289930/v1>

**License:** © ⓘ This work is licensed under a Creative Commons Attribution 4.0 International License.

[Read Full License](#)

---

# Abstract

This study examines the turbulent flow field and heat transfer rate (HTR) of the non-Newtonian H<sub>2</sub>O-Al<sub>2</sub>O<sub>3</sub>-carboxymethyl (CMC) in a channel with vortex generators. The finite volume method and SIMPLE algorithm were employed for solving the partial differential equations. The mean Nusselt numbers (Num) and pressure drops were studied at angles of 30-60°, vortex generator depths of 1-3 mm, Reynolds numbers (Re) of 3000-30000, and nanoparticles volume fractions ( $\varphi$ ) of 0.5% and 1.5%. According to the numerical results, the use of triangular vortex generators significantly incremented the Nusselt number (Nu) of the non-Newtonian nanofluid (NF), while it had a lower effect on the enhancement of pressure drop (DP). It was also indicated that a change in the vortex generator depth in the range of a few millimeters had no significant effects on the Nu and pressure drop. Moreover, a rise in the Re (i.e., more turbulent flow) significantly incremented HTR. An increase in the Re raised pressure drop; however, the Num incremented more than the pressure drop. Also, the variations of the local Nu indicated that the local Nu significantly incremented around vortex generators due to the formation of vortex flows. An enhancement in the volume fraction of the base fluid's nanoparticles (NPs) from 0.5% to 1.5% significantly incremented HTR and the Nu.

## 1. Introduction

Because of the importance of HTR in many industrial phenomena such as energy consumption management [1-8], heat storage [9,10], cooling [11-14], and desalination [15,16], numerous scientists have focused on HTR enhancement. The distribution of vortex generations is widely employed to enhance HTR in heat exchangers and the cooling of turbine blades and electronic pieces. Considering the importance of vortex generators in improving HTR, they have been used to break thermal layers and increment turbulence in many cases. The use of vortex generators on surface walls has been considered as a passive HTR method. When a fluid flows through a channel with vortex generators, the flow becomes turbulent due to the growth of rotational regions near the vortex generators, leading to the NF mixture and HTR improvement. Parsaei et al. [17] simulated the turbulent flow and HTR of the Al<sub>2</sub>O<sub>3</sub>-H<sub>2</sub>O NF in a rectangular vortex generator channel. They examined the impacts of the vortex generator angle of attack in a rectangular channel, Re, and Nu of the NPs on HTR enhancement. The results showed that the Nu incremented by 2.37, 1.96, and 2 times at the Re ranging from 15000 to 30000 and an attack angle of 60° compared to an attack angle of 0°, respectively. Toghraei et al. [18] numerically studied a flow and HTR in flat, sine-shaped, and angled microchannels with and without a NF. They employed the amplitude and microchannel length, the sine shape of waves and vortex generators,  $\varphi$ , and Re on HTR as the performance evaluation criteria of the channel. The results demonstrated that the use of sin-shaped microchannels without a NF is more effective than the use of NPs in flat microchannels in cases where only HTR is considered. By analyzing the effects of the wavelength and amplitude on the Nu, it was found that a decline in the sine wavelength and rib length would raise the Nu. It was also indicated that the use of zigzag vortex generators in the channel produced better performance than the use of sine waves. Toghraei et al. [19] studied the effects of employing the CuO-H<sub>2</sub>O NF and L-shaped porous vortex

generators on microchannel performance evaluation criteria. In addition to the pure H<sub>2</sub>O, the effects of using the CuO-H<sub>2</sub>O NF on the microchannel were examined. Flows were simulated at four Re and two  $\phi$ . The results indicated that the NF had no significant effects on the enhancement of HTR, despite porous ribs. The use of porous vortex generators improved the HTR to 42% and 25% at the Re of 1200 and 100, respectively. Hamdi et al. [20] improved the HTR of NF flow with a turbulent flow regime in a channel with triangular vortex generators on the wall. They included parameters such as NP type, NP content, NP diameter, and Re to indicate their effects on the HTR coefficient and friction coefficient. The NP contents of 1-6% and the Re of 4000-32000 were included. The results demonstrated that the  $Nu_m$  was 84.45% higher at a Re of 32000 than at a Re= 4000 and  $\phi=6\%$  for the ethylene glycol-SiO<sub>2</sub> NF. The results also showed that a rise in the NP concentration exerted a slight rise in the friction coefficient. Ahmad et al. [21] numerically studied the flow features and HTR of the H<sub>2</sub>O-CuO NF within direct channels with sine, triangular, and trapezoidal vortex generators. The effects of the  $\phi$  and Re on the flow velocity, temperature contour,  $Nu_m$ , dimensionless DP, and thermal-hydraulic performance were examined. The results demonstrated that the  $Nu_m$  and thermal-hydraulic performance rose as the  $\phi$  and Re increment for all the channel shapes. Also, they reported the trapezoidal channel to have the largest Nu, followed by sine, triangular, and direct channels, respectively. Raghoub and Mansouri [22] analytically investigated the forced convection flow of a non-Newtonian fluid in a channel with an oval cross-section. They considered the input fluid temperature as an alternating function of the temperature. They also employed a power model to describe non-Newtonian fluid's behavior. The results revealed the significant effects of the shape factor and the power equation's powers on the reduction of the temperature variation range. Tehrani et al. [23] evaluated the convective HTR of the non-Newtonian CuO-carboxymethyl (CMC) NF in a tube equipped with a spiral band. They showed that the NF's behavior was similar to that of pseudoplastic fluids. According to their results, the use of the spiral band improved the HTR and DP; however, HTR improvement dominated DP rise. Ghorbani and Javaherdeh [24] studied improving the thermal efficiency of non-Newtonian NF flow in a baffled porous environment. They selected CMC cellulose as the base fluid, solving the problem for the  $\phi=0.05\%$ , 0.1%, and 0.2%. Their variables included the Nu, friction coefficient, and thermal efficiency. The results revealed that adding 0.2 wt.% of carbon nanotubes to the base fluid improved the mean conductivity coefficient and heat transfer coefficient (HTC) by 12.4% and 39.4%, respectively. The results also indicated that the use of a non-Newtonian NF flow along with a porous environment could improve the thermal efficiency by up to 29%. Lamaroei et al. [25] numerically examined the thermal and dynamic behavior of the non-Newtonian H<sub>2</sub>O-Al<sub>2</sub>O<sub>3</sub> NF. They solved the problem for the volumes fractions of 0-5% and the Re of 25-300. Also, they employed Stowald's model to model the NF's flow behavior. The variables included the HTC,  $Nu_m$ , streamlines, and isothermal contours at different Re. They demonstrated that an enhancement in the Re and  $\phi$  in the base fluid incremented HTR. They also showed that the required pumping power of a non-Newtonian fluid was significantly larger than that of a Newtonian fluid in the same conditions. Rashed et al. [26] numerically studied the non-Newtonian CuO-CMC NF in a fined microchannel. They examined the hydrodynamic behavior and entropy generation of the non-Newtonian NF. The results indicated the optimal ratio of HTR to DP to be nearly 2.29. Also, NF's entropy generation was 2.7% lower than that of the base fluid in the

optimal conditions. Lee et al. [27] numerically evaluated the HTR efficiency of a non-Newtonian fluid in a microchannel. They simulated the problem in a three-dimensional setting and employed the power law to simulate the non-Newtonian fluid's behavior.

Sajjadifar et al. [28] investigated the flow field and HTR of a non-Newtonian NF in micro-tubes with the velocity sliding condition and temperature jump. They evaluated the effects of the  $\phi$ . They demonstrated that a rise in the Re, sliding coefficient and  $\phi$  raised the dimensionless Nu. Aliakbari et al. [29] studied the effects of NP velocity and size on the HTR of non-Newtonian NF flow. They limited their work to laminar flows, a Re range of 10-100, and  $\phi=0.5\%$  and  $1.5\%$ . Geravandian et al. [30] investigated the effects of the vortex generator shape factor on the HTR of the non-Newtonian H<sub>2</sub>O-TiO<sub>2</sub> NF flow in a two-dimensional rectangular microchannel. They limited their work to laminar flows, Re of 10, 50, 100, and 300, and  $\phi=0\%$ ,  $2\%$ , and  $4\%$  for shape factors of 10, 15, 20, and 25. The results revealed that a rise in the  $\phi$  in the base fluid enhanced HTR, friction coefficient, efficiency evaluation index, and DP. They also indicated that the friction coefficient was almost independent of the shape factor but was a function of the  $\phi$ . Shamsaei et al. [31] evaluated the HTR of a non-Newtonian NF's flow in a rectangular microchannel with triangular vortex generators. They employed the power-law model to model the non-Newtonian fluid's flow. The results showed that the use of triangular ribs with an angle of  $30^\circ$  lead to the maximum Nu rise and minimum DP. Rahmati et al. [32] simulated the flow of a non-Newtonian NF with different  $\phi$  in the base fluid and sliding and non-sliding boundary conditions. They applied the power-law model for simulating the non-Newtonian fluid's behavior. The results suggested that an enhancement in the  $\phi$  and velocity sliding factor reduced the temperature gradient in the layers near the fluid surface. Nike and Windod [33] studied the forced convective HTR enhancement of a non-Newtonian NF within a shell and tube heat exchanger with a spiral coil. They investigated FeO, Al<sub>2</sub>O<sub>3</sub>, and CuO NPs in a CMC base fluid. The results demonstrated that a rise in the  $\phi$  incremented the shell=side temperature and Nu<sub>m</sub>. Also, the use of CuO as for NPs yielded the highest performance. Sun et al. [34] studied the convective HTR of the non-Newtonian H<sub>2</sub>O-Al<sub>2</sub>O<sub>3</sub> NF flow at  $\phi=0$  to  $3\%$ . They used the power model to simulate the non-Newtonian fluid's behavior. Rashed et al. [35] numerically studied the flow of the non-Newtonian CuO-CMC in a finned microchannel. They evaluated the effects of the  $\phi$  in the base fluid, Re, and fin shape on the thermal performance from the first and second laws of thermodynamics. Javadpour et al. [36] experimentally investigated the effects of a magnetic field on the forced convective HTR of a non-Newtonian NF within a channel. They evaluated laminar and steady flows subjected to a fixed magnetic field and constant heat flux. They employed the CMC-H<sub>2</sub>O combination as the base fluid, reporting that an enhancement in the  $\phi$  in the base fluid enhanced local HTR. They also found that the presence of a fixed magnetic field incremented the mean HTC by  $13\%$  for the NF with  $\phi=1\%$ .

The previous studies indicate that no study investigated the turbulent flow field and HTR of the non-Newtonian H<sub>2</sub>O-Al<sub>2</sub>O<sub>3</sub>-CMC NF in a channel with triangular vortex generators. The present study investigates the effects of angles of  $30^\circ$ - $60^\circ$ , vortex generator depths of 1-3 mm, Re of 3000-30000, and  $\phi=0.5$  to  $1.5\%$  on the Nu<sub>m</sub> and flow field.

## 2. Geometry And Nf Properties

Fig. 1 illustrates the channel with triangular vortex generators. Also, Table 1 represents the included geometry.

**Table 1.** Channel dimensions with different attack angles

Parameters	Value		
$L_2 (mm)$	1500	1500	1500
$L_3 (mm)$	1500	1500	1500
$H (mm)$	40	40	40
$P (mm)$	3	3	3
$Z (mm)$	1	2	3
$\theta (deg)$	30	45	60

The flow was considered as a two-dimensional, incompressible, non-Newtonian, turbulent, and single-phase flow. The properties of non-Newtonian NF were used at the fixed temperature. The flow was assumed to enter uniformly at a fixed velocity, and the NPs were treated as completely spherical. The flow field and HTR were numerically solved for all Re and hydrodynamic development conditions. The power model was employed to simulate the non-Newtonian NF. The constants of the power model were extracted from the data provided by [25]. Also, non-Newtonian fluid coefficients (i.e.,  $n$  and  $k$ ) were treated to remain unchanged for each nanoparticles concentration. The non-Newtonian  $H_2O-Al_2O_3$ -CMC NF was included. Table 2 provides the thermophysical characteristics of the base fluid,  $Al_2O_3$  NPs, and  $H_2O-Al_2O_3$ -CMC NF.

**Table 2.** The thermophysical characteristics of the base fluid, NPs, and NF at different volume fractions [24]

Material	$\rho \left( \frac{kg}{m^3} \right)$	$C_p \left( \frac{J}{kg.K} \right)$	$\lambda \left( \frac{W}{m.K} \right)$
Water	997.1	4179	0.613
$Al_2O_3$	3970	765	40
CMC(0.5%)+1%+ $Al_2O_3$	1013.5	4121	0.6157
CMC(0.5%)+1.5%+ $Al_2O_3$	1040.5	4012	0.6823

$\lambda$  is the thermal conductivity coefficient. The channel walls are subjected to a fixed heat flux. Also, Figs. 2 and 3 demonstrate  $n$  and  $k$  values for the non-Newtonian NF at different temperatures and volume fractions, respectively.

## 3. Governing Equations

The continuity and momentum conservation equations are written as

$$\frac{\partial u}{\partial x} + \frac{\partial v}{\partial y} + \frac{\partial w}{\partial z} = 0 \quad (1)$$

$$\rho \left( u \frac{\partial u}{\partial x} + v \frac{\partial u}{\partial y} + w \frac{\partial u}{\partial z} \right) = \frac{\partial \sigma_x}{\partial x} + \frac{\partial \tau_{yx}}{\partial y} + \frac{\partial \tau_{zx}}{\partial z} \quad (2)$$

$$\rho \left( u \frac{\partial v}{\partial x} + v \frac{\partial v}{\partial y} + w \frac{\partial v}{\partial z} \right) = \frac{\partial \sigma_y}{\partial y} + \frac{\partial \tau_{xy}}{\partial x} + \frac{\partial \tau_{zy}}{\partial z} \quad (3)$$

where C, D, E, F, G, and H are defined as [24]

$$\tau_{xy} = k \left( \frac{\partial u}{\partial y} \right)^n \quad (4)$$

$$\tau_{xz} = k \left( \frac{\partial u}{\partial z} \right)^n \quad (5)$$

$$\tau_{yz} = k \left( \frac{\partial v}{\partial z} \right)^n \quad (6)$$

$$F = 2 \left( \frac{\Pi}{2} \right)^{\frac{n-1}{2}} \frac{\partial v}{\partial y} \quad (7)$$

$$G = \left( \frac{\Pi}{2} \right)^{\frac{n-1}{2}} \left( \frac{\partial v}{\partial z} + \frac{\partial w}{\partial y} \right) \quad (8)$$

$$H = 2 \left( \frac{\Pi}{2} \right)^{\frac{n-1}{2}} \frac{\partial w}{\partial z} \quad (9)$$

$$\frac{\Pi}{2} = 2 \left[ \left( \frac{\partial u}{\partial x} \right)^2 + \left( \frac{\partial v}{\partial y} \right)^2 + \left( \frac{\partial w}{\partial z} \right)^2 \right] + \left( \frac{\partial u}{\partial y} + \frac{\partial v}{\partial x} \right)^2 + \left( \frac{\partial w}{\partial y} + \frac{\partial v}{\partial z} \right)^2 + \left( \frac{\partial u}{\partial z} + \frac{\partial w}{\partial x} \right)^2 \quad (10)$$

The Reynolds, Peclet, and Prandtl number are defined as [24]

$$Re = \frac{\rho U^{2-n} D^n}{k} \quad (11)$$

$$Pr = \frac{c_{p,nf}}{k_{nf}} \left( \frac{V_{nf}}{D_h} \right)^{n-1} \quad (12)$$

in which  $\nu$  is the kinematic viscosity. Also, the local convective HTC is defined as

$$h(x) = \frac{q''}{T_w - T_{in}} \quad (19)$$

where  $T_w$ ,  $T_{in}$ , and  $q''$  denote the local wall temperature, mean input fluid temperature, and heat flux on the wall, respectively. Also,  $\bar{h}$  is the mean convective HTC. The  $Nu_m$  is calculated as

$$Nu_{avg} = \frac{\bar{h} \times D_h}{k_f} \quad (20)$$

## 4. Numerical Simulation

The governing equations have been solved by the finite volume method and the SIMPLE procedure. A uniform grid was applied to the solving field. Then, control volumes were created around the nodes. The governing equations were integrated, separating the equations and obtaining a system of algebraic equations. The second-order central difference was used for distribution terms, while the hybrid method was applied to displacement terms. The central difference method was employed for Peclet numbers below 0.2, while the upstream method was used for Peclet numbers above 2. The under-relaxation factors of 0.5 and 0.7 were employed for the velocity components and temperature to obtain convergence.

### 4.1. Validation

The numerical results provided by Akbari et al. [29] were used to validate the proposed numerical model. Akbari et al. [29] numerically studied the flow of a non-Newtonian NF composed of H<sub>2</sub>O and 0.5 wt.% CMC at  $\phi=0.5\%$  and  $1.5\%$  in a rectangular channel. They evaluated laminar flows. Fig. 4 compares the numerical results provided by Akbari et al. [29] to those provided by the present work. This study's results are provided for the Re of 100 and 500 (laminar flows) and a  $\phi=1.5\%$ . As can be seen, the numerical results are in good agreement, suggesting the accuracy of the proposed numerical model.

### 4.2. Grid-independence of the results

This section investigates the grid-independence of the solution. Generally, grid-independence indicates that the reduction of meshing elements (i.e., increasing the number of elements) does not significantly

change the numerical results, i.e., result changes are ignorable in comparison to the reduction of computational efforts. The present study employed 5000-12000 structured rectangular meshes to investigate grid-independence. Table 3 provides the friction coefficient and Nu for the lower wall in the first sample at  $\varphi=1.5\%$  for different meshes.

**Table 3.** Grid-independence evaluation

Number of elements	$Nu_{ave}$	$C_{f,ave}$
5000	35.1987	0.38609
7500	35.2731	0.3870
60000	36.1001	0.38813
90000	36.2864	0.38964
120000	36.2976	0.38976

According to Table 3, the solution becomes independent from the grid for a grid number of 600000, with an error of smaller than 5%.

## 5. Result Analysis

### 5.1. Flow field

Figs. 5 and 6 illustrate the NF's velocity distributions at fraction volumes of 0.5% and 1.5% for a Re of 5000 and three different triangular vortex generator angles, respectively. As can be seen, the maximum velocity occurs on the right side of the vortex generators' tips at the attack angles of 30° and 45°. However, a rise in the attack angle shifts the maximum velocity location backwards. Also, very few abrupt changes are observed in the velocity contour at the attack angles of 30° and 45°. As can be seen, at the attack angle of 60°, some vortexes form behind the vortex generators, leading to abrupt velocity changes on the contact surface of the vortex generators and the fluid on them. Considering the abrupt thinning of the channel due to the vortex generators in the flow direction (particularly at the attack angle of 60°), the channel's effective cross-section reduces, increasing the maximum fluid velocity in vortex generator locations. Considering the gradual change in the slopes of the vortex generators at the attack angles of 30° and 45°, the velocity contour is symmetric, as shown in Figs. 5 and 6. For the attack angle of 60°, however, the velocity contour is observed to be asymmetric due to dramatic and abrupt slope changes. Changes in the velocity can influence the growth of the boundary layer formed next to the vortex generator due to the attack angle change. This negative effect is higher for the attack angle of 60°.

### 5.2. Temperature field

Fig. 7 demonstrates the static temperature distribution contour at  $\varphi=1.5\%$  and Re= 5000 for three attack angles. The temperature change contour is indicated for different layers of the fluid, from locations near the warm wall to the surrounding of the channel's upper wall, for vortex generator attack angles. For the

attack angles of  $30^\circ$  and  $45^\circ$ , the static temperature change (thermal boundary layer growth) gradually reduces as the fluid moves toward the vortex generator tip in the upper locations of the warm wall, but it begins to rise after the vortex generator. In fact, it can be said that the mentioned locations represent warm locations or locations with low HTR, and the growth of such locations should reduce to some extent, so HTR would increment. However, the growth of the thermal boundary layer is inevitable due to the effect of HTR from the warm wall to the cold wall in the middle part of the channel. Unlike the attack angles of  $40^\circ$  and  $60^\circ$ , the thermal boundary layer's growth before and after the vortex generator is considerably smaller for the attack angle of  $30^\circ$ , which increments HTR at this angle. However, the temperature gradient behind the vortex generator dramatically incremented for the attack angle of  $60^\circ$ , while the static temperature does not show a symmetric rise before and after the vortex generator. This created some warm locations with low HTC. This is a drawback of channels with vortex generators, which is resolved by selecting suitable attack angles for vortex generators.

### 5.3. Local Nu variations

Fig. 8 illustrates the local Nu variations in the channel direction for an attack angle of  $30^\circ$  at different Re. Also, Figs. 9 and 10 demonstrate the local Nu variations in the channel direction at different Re and vortex generator heights. As can be seen in Fig. 8, the maximum Nu occurs in the channel's inlet for all the cases because no thermal boundary layer has formed in the inlet yet, and the highest temperature difference exists between the channel surface and NF, which rationally enhances HTR and the Nu. As the fluid flow passes through the channel, a thermal boundary layer forms and grows, reducing the temperature gradient slope. As can be seen, the reduction trend begins after the channel's inlet. It can also be understood that the local Nu takes a larger value in the vortex generator tip for all the cases. The cross-section decreases as the vortex generators' tips are approached, enhancing the flow velocity. The flow velocity continues to enhance up to the vortex generator tip, where HTR reduces due to the inverse vortex generator slope and reduced velocity. Concerning the local Nu graphs, it should be noted that the Nu of the vortex generator tip reduces by moving forward through the channel.

Because the fluid exchanges heat with the wall while passing through the channel, the fluid temperature decreases in the channel direction, with the temperature gradient between the channel surface and fluid reducing. This reduces local Nu. Also, Fig. 8 implies that a rise in the Re raises the Nu in the channel direction, leading to improved HTR. This is more obvious around the vortex generators because the velocity rises as the fluid flows on the vortex generator due to the cross-section reduction, enhancing the Re, and HTR rises as the flow becomes more turbulent, vortexes form, and the thermal boundary layer disappears.

The same case holds for the Nu in all the situations. According to the local Nu graphs, a change in the attack angle and vortex generator shape considerably influences HTR improvement. The variations of the local Nu near the vortex generators are observed by comparing Figs. 4-12 and 4-14.

### 5.4. Mean Nu variations

Fig. 11 shows  $Nu_m$  variations at the Re of 5000, 15000, and 30000 for different attack angles, vortex generation depths, and volume fractions. As can be seen, a rise in the  $\varphi$  raises the Nu for all the vortex generator depths. In fact, as the  $\varphi$  increment, the NF's thermal conductivity coefficient increments, enhancing HTR. Also, it can be found that the  $Nu_m$  decreases as the attack angle increments. The presence of obstacles helps the fluid to be mixed more effectively near the warm zone, producing vortices. Such vortices separate the warm fluid near the wall and replace it with cold fluid, improving HTR and enhancing the Nu. However, the incremented vortex generator attack angle brings abrupt changes onto the channel surface. Therefore, more powerful vortices form, and HTR improves. For a fixed vortex generator height, however, a rise in the triangular vortex generator's attack angle decreases the  $Nu_m$  because the heat exchange area reduces for a larger attack angle.

## 5.5. Pressure drop variations

Fig. 12 represents DP variation for different Re, different triangular vortex generator heights, and two  $\varphi$ . At the attack angles, a rise in the  $\varphi$  often raises DP due to the incremented number of NPs and high power coefficient  $k$  for a non-Newtonian fluid with a higher  $\varphi$ . Moreover, the incremented  $k$  helps the adhesive force overcome the inertia force, leading to the fluid being more influenced by the adhesive force. Therefore, the DP of the NF with  $\varphi=1.5\%$  is larger than that of the NF with  $\varphi=0.5\%$ . According to Fig. 12, the vortex generator profile has no significant effect on DP for low Re. However, this effect becomes larger for high Re (e.g., 15000 and 30000). A larger DP occurs for the attack angle of  $60^\circ$  within the channel. An abrupt change in the area forms powerful vortices and increments DP. The triangular vortex generator's DP variation is larger at  $\varphi=0.5\%$  than at  $\varphi=1.5\%$  because of the apparent viscosity of the non-Newtonian NFs. In fact, the apparent viscosity of a non-Newtonian fluid is not only a function of  $k$  and  $n$  in the power model but is also a function of the fluid's shear stress. For fixed  $k$  and  $n$  values, a rise in the fluid's stress enhances the apparent viscosity. As the vortex generator attack angle rises, the fluid flow abruptly changes in the vortex generator zone, leading to a larger DP, particularly at an attack angle of  $60^\circ$ . In this case, the apparent viscosity can be calculated using the power model.

According to Fig. 12, a change in the vortex generator depth slightly changes the DP due to the incremented shear stress and more turbulent flow. However, such changes are small. A change in the  $\varphi$  in the base fluid has a more significant effect on the DP because a rise in the  $\varphi$  raises the apparent viscosity, leading to a larger DP.

## 6. Conclusion

The present study investigated the turbulent flow and HTR of a non-Newtonian fluid in a channel with triangular vortex generators. The  $Nu_m$  and DP were studied for the attack angles of  $30^\circ$ ,  $45^\circ$ , and  $60^\circ$ , vortex generator depths of 1-3 mm, Re of 3000-30000, and  $\varphi=0.5\%$  and  $1.5\%$ . The most important numerical results included

1. The use of triangular vortex generators significantly enhanced the Nu, while it had a smaller effect on the DP rise.
2. An enhancement in the Re (i.e., a more turbulent flow) significantly enhanced HTR (mean dimensionless Nu). The incremented Re also incremented the DP. However, the Nu underwent a more significant rise than the DP.
3. The variations of the local Nu indicated that the local Nu significantly incremented near the vortex generators due to the formation of vortex flows.
4. For low Re, the vortex generator profile had a small effect on the DP; however, the effect became larger for higher Re (e.g., 15000 and 30000).
5. The DP of the triangular vortex generators was larger at  $\varphi=0.5\%$  than at  $\varphi=1.5\%$  due to the apparent viscosity of non-Newtonian NFs.
6. A larger DP occurred for an attack angle of  $60^\circ$  within the channel.
7. As the vortex generator attack angle incremented, the fluid flow abruptly changed in the vortex generator zone, leading to a larger DP, particularly for an attack angle of  $60^\circ$ .
8. For an attack angle of  $60^\circ$ , some vortexes formed behind the vortex generators, leading to abrupt changes in the velocity on the vortex generator contact surface.

## References

- [1]W. Liu, R. Kalbasi, and M. Afrand, "Solutions for enhancement of energy and exergy efficiencies in air handling units," *Journal of Cleaner Production*, vol. 257, p. 120565, 2020/06/01/ 2020
- [2]R. Kalbasi, F. Izadi, and P. Talebizadehsardari, "Improving performance of AHU using exhaust air potential by applying exergy analysis," *Journal of Thermal Analysis and Calorimetry*, 2020/01/20 2020
- [3]M. Yari, R. Kalbasi, and P. Talebizadehsardari, "Energetic-exergetic analysis of an air handling unit to reduce energy consumption by a novel creative idea," *International Journal of Numerical Methods for Heat & Fluid Flow*, vol. 29, pp. 3959-3975, 2019
- [4]R. Kalbasi, A. Shahsavari, and M. Afrand, "Incorporating novel heat recovery units into an AHU for energy demand reduction-exergy analysis," *Journal of Thermal Analysis and Calorimetry*, 2019/12/05 2019
- [5]R. Kalbasi, A. Shahsavari, and M. Afrand, "Reducing AHU energy consumption by a new layout of using heat recovery units," *Journal of Thermal Analysis and Calorimetry*, 2019/12/06 2019
- [6]R. Kalbasi, B. Ruhani, and S. Rostami, "Energetic analysis of an air handling unit combined with enthalpy air-to-air heat exchanger," *Journal of Thermal Analysis and Calorimetry*, 2019/12/12 2019
- [7]Z. X. Li, A. Shahsavari, A. A. A. Al-Rashed, R. Kalbasi, M. Afrand, and P. Talebizadehsardari, "Multi-objective energy and exergy optimization of different configurations of hybrid earth-air heat exchanger

- and building integrated photovoltaic/thermal system," *Energy Conversion and Management*, vol. 195, pp. 1098-1110, 2019/09/01/ 2019
- [8]Z. X. Li, A. A. A. Al-Rashed, M. Rostamzadeh, R. Kalbasi, A. Shahsavar, and M. Afrand, "Heat transfer reduction in buildings by embedding phase change material in multi-layer walls: Effects of repositioning, thermophysical properties and thickness of PCM," *Energy Conversion and Management*, vol. 195, pp. 43-56, 2019/09/01/ 2019
- [9]S. Gholipour, M. Afrand, and R. Kalbasi, "Improving the efficiency of vacuum tube collectors using new absorbent tubes arrangement: Introducing helical coil and spiral tube adsorbent tubes," *Renewable Energy*, 2019
- [10]A. A. Nadooshan, R. Kalbasi, and M. Afrand, "Perforated fins effect on the heat transfer rate from a circular tube by using wind tunnel: An experimental view," *Heat and Mass Transfer*, vol. 54, no. 10, pp. 3047-3057, 2018
- [11]R. Kalbasi and M. R. Salimpour, "Constructal design of horizontal fins to improve the performance of phase change material rectangular enclosures," *Applied Thermal Engineering*, vol. 91, pp. 234-244, 2015/12/05/ 2015
- [12]R. Kalbasi and M. R. Salimpour, "Constructal design of phase change material enclosures used for cooling electronic devices," *Applied Thermal Engineering*, vol. 84, pp. 339-349, 2015/06/05/ 2015
- [13]M. R. Salimpour, R. Kalbasi, and G. Lorenzini, "Constructal multi-scale structure of PCM-based heat sinks," *Continuum Mechanics and Thermodynamics*, vol. 29, no. 2, pp. 477-491, 2017
- [14]R. Kalbasi, M. Afrand, J. Alsarraf, and M.-D. Tran, "Studies on optimum fins number in PCM-based heat sinks," *Energy*, vol. 171, pp. 1088-1099, 2019
- [15]R. Kalbasi, A. A. Alemrajabi, and M. Afrand, "Thermal modeling and analysis of single and double effect solar stills: An experimental validation," *Applied Thermal Engineering*, vol. 129, pp. 1455-1465, 2018/01/25/ 2018
- [16]E. Shanazari and R. Kalbasi, "Improving performance of an inverted absorber multi-effect solar still by applying exergy analysis," *Applied Thermal Engineering*, vol. 143, pp. 1-10, 2018
- [17] Parsaiemehr, Mohammad, et al. "Turbulent flow and heat transfer of Water/Al<sub>2</sub>O<sub>3</sub> NF inside a rectangular ribbed channel." *Physica E: Low-Dimensional Systems and Nanostructures* 96 (2018): 73-84.
- [18] Toghraie, Davood, et al. "Numerical investigation of flow and heat transfer characteristics in smooth, sinusoidal and zigzag-shaped microchannel with and without NF." *Journal of Thermal Analysis and Calorimetry* 131.2 (2018): 1757-1766.

- [19] Toghraie, Davood, et al. "The effect of using water/CuO NF and L-shaped porous ribs on the performance evaluation criterion of microchannels." *Journal of Thermal Analysis and Calorimetry* 135.1 (2019): 145-159.
- [20] Ahmed, Hamdi E., B. H. Salman, and A. Sh Kerbeet. "Heat transfer enhancement of turbulent forced NF flow in a duct using triangular rib." *International Journal of Heat and Mass Transfer* 134 (2019): 30-40.
- [21] Ahmed, M. A., et al. "Effect of corrugation profile on the thermal–hydraulic performance of corrugated channels using CuO–water NF." *Case Studies in Thermal Engineering* 4 (2014): 65-75.
- [22] Al-Rashed, Abdullah AAA, et al. "Numerical investigation of non-Newtonian water-CMC/CuO NF flow in an offset strip-fin microchannel heat sink: thermal performance and thermodynamic considerations." *Applied Thermal Engineering* 155 (2019): 247-258.
- [23] Ahmed, Hamdi E., B. H. Salman, and A. Sh Kerbeet. "Heat transfer enhancement of turbulent forced NF flow in a duct using triangular rib." *International Journal of Heat and Mass Transfer* 134 (2019): 30-40.
- [24] Bazdidi-Tehrani, Farzad, Seyed Mehdi Khanmohamadi, and Seyed Iman Vasefi. "Evaluation of turbulent forced convection of non-Newtonian aqueous solution of CMC/CuO NF in a tube with twisted tape inserts." *Advanced Powder Technology* (2020).
- [25] Ghanbari, Shahin, and Kourosh Javaherdeh. "Thermal performance enhancement in perforated baffled annuli by nanoporous graphene non-Newtonian NF." *Applied Thermal Engineering* 167 (2020): 114719.
- [26] Lamraoui, Hanan, Kacem Mansouri, and Rachid Saci. "Numerical investigation on fluid dynamic and thermal behavior of a non-Newtonian Al<sub>2</sub>O<sub>3</sub>–water NF flow in a confined impinging slot jet." *Journal of Non-Newtonian Fluid Mechanics* 265 (2019): 11-27.
- [27] Li, Si-Ning, et al. "Numerical study on the heat transfer performance of non-Newtonian fluid flow in a manifold microchannel heat sink." *Applied Thermal Engineering* 115 (2017): 1213-1225.
- [28] Sajadifar, Seyed Ali, Arash Karimipour, and Davood Toghraie. "Fluid flow and heat transfer of non-Newtonian NF in a microtube considering slip velocity and temperature jump boundary conditions." *European Journal of Mechanics-B/Fluids* 61 (2017): 25-32.
- [29] Akbari, Omid Ali, et al. "The effect of velocity and dimension of solid NPs on heat transfer in non-Newtonian NF." *Physica E: Low-Dimensional Systems and Nanostructures* 86 (2017): 68-75.
- [30] Gravndyan, Qumars, et al. "The effect of aspect ratios of rib on the heat transfer and laminar water/TiO<sub>2</sub> NF flow in a two-dimensional rectangular microchannel." *Journal of Molecular Liquids* 236 (2017): 254-265.

[31] Shamsi, Mohammad Reza, et al. "Increasing heat transfer of non-Newtonian NF in rectangular microchannel with triangular ribs." *Physica E: Low-Dimensional Systems and Nanostructures* 93 (2017): 167-178.

[32] Rahmati, Ahmad Reza, et al. "Simultaneous investigations the effects of non-Newtonian NF flow in different volume fractions of solid NPs with slip and no-slip boundary conditions." *Thermal Science and Engineering Progress* 5 (2018): 263-277.

[33] Naik, B. Anil Kumar, and A. Venu Vinod. "Heat transfer enhancement using non-Newtonian NFs in a shell and helical coil heat exchanger." *Experimental Thermal and Fluid Science* 90 (2018): 132-142.

[34] Sun, Meng-He, Guan-Bang Wang, and Xin-Rong Zhang. "Rayleigh-Bénard convection of non-Newtonian NFs considering Brownian motion and thermophoresis." *International Journal of Thermal Sciences* 139 (2019): 312-325.

[36] Al-Rashed, Abdullah AAA, et al. "Numerical investigation of non-Newtonian water-CMC/CuO NF flow in an offset strip-fin microchannel heat sink: thermal performance and thermodynamic considerations." *Applied Thermal Engineering* 155 (2019): 247-258.

[36] Javadpour, Ally, Mohammad Najafi, and Kourosh Javaherdeh. "Effect of magnetic field on forced convection heat transfer of a non-Newtonian NF through an annulus: an experimental study." *Heat and Mass Transfer* 54.11 (2018): 3307-3316.

## Figures

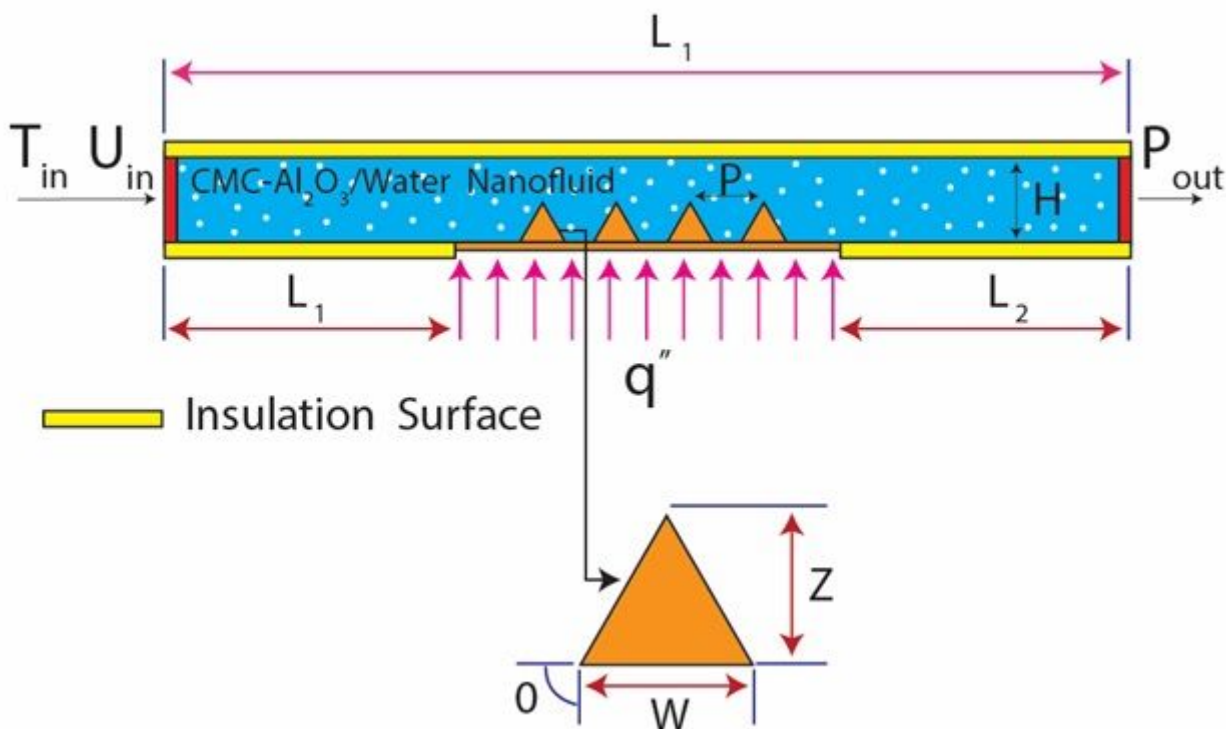


Figure 1

A schematic of the geometry

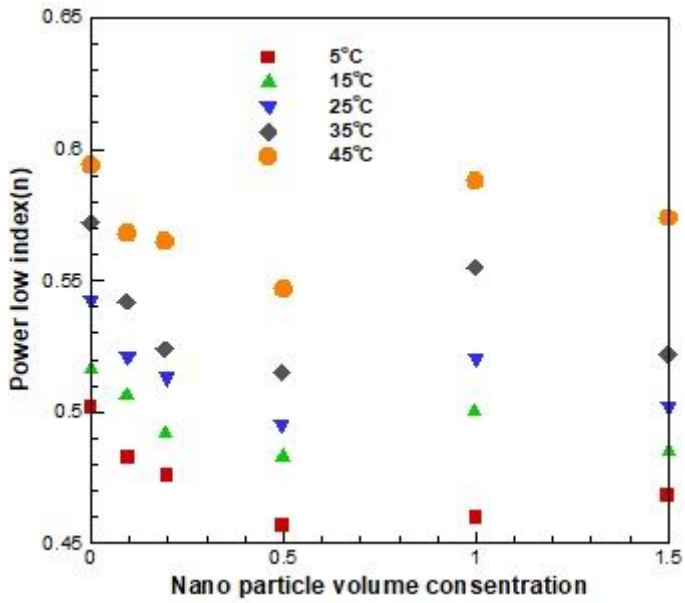


Figure 2

n values for the NF in the power model [25]

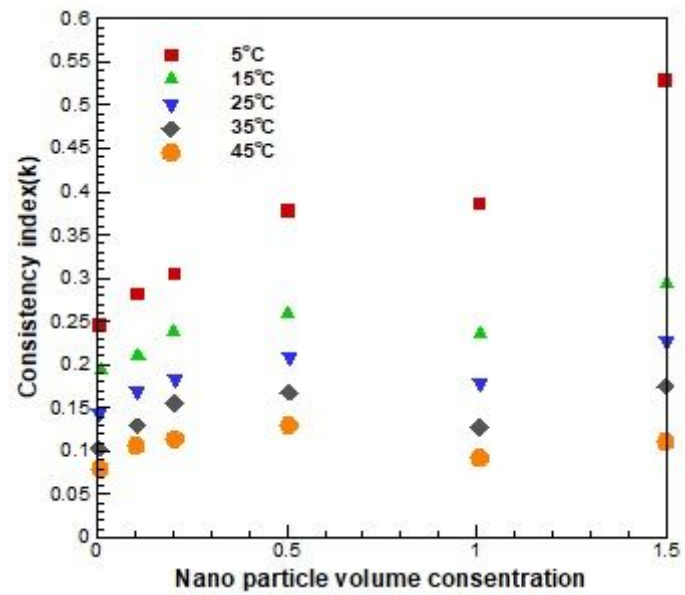


Figure 3

k values for the NF in the power model [25]

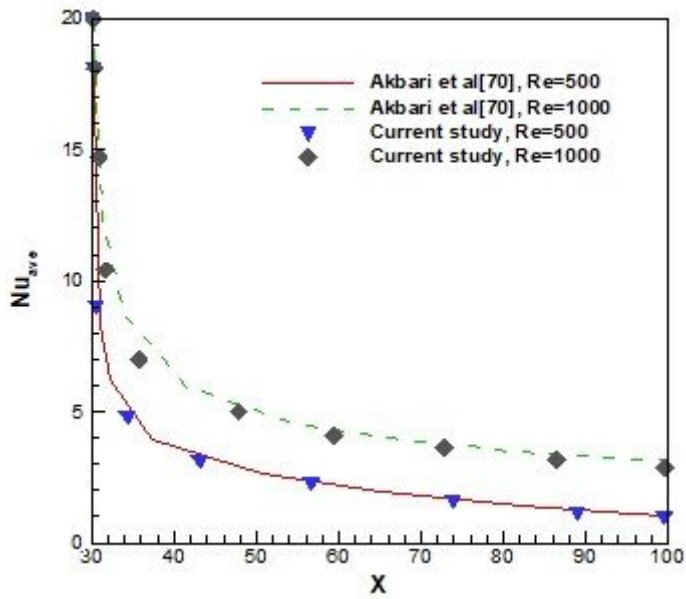


Figure 4

Numerical solution validation through Akbari et al. [29]

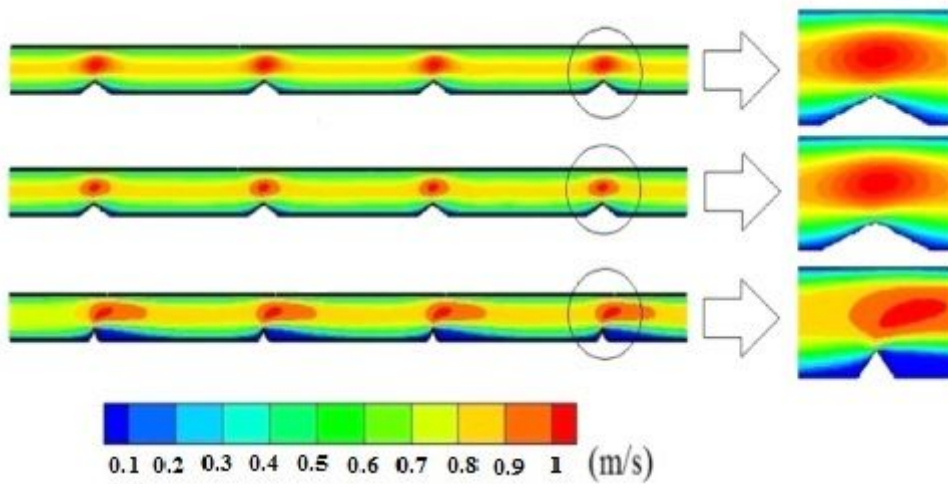
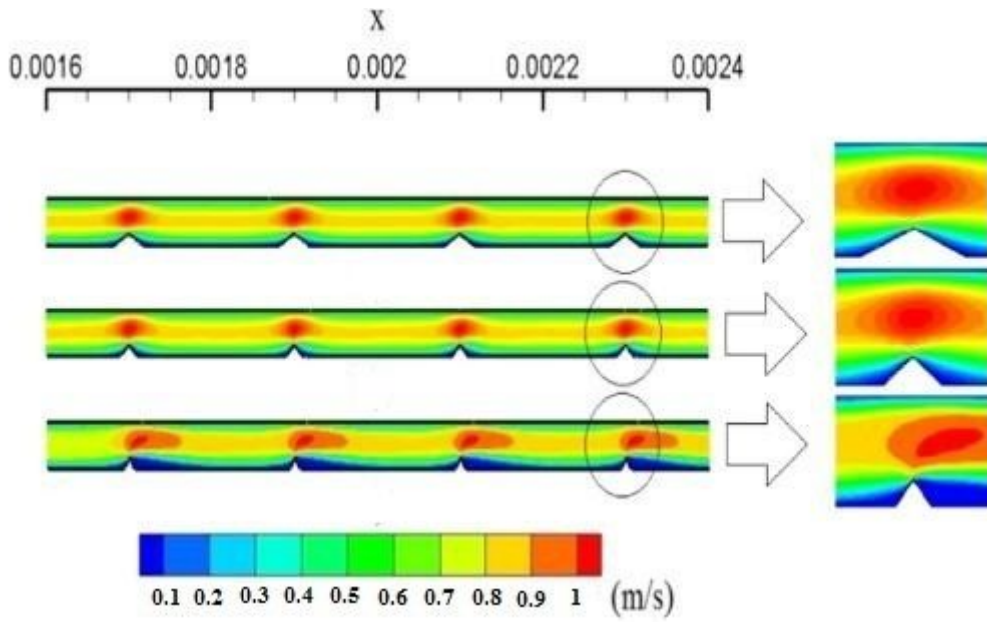


Figure 5

The NF velocity distribution at  $\varphi=0.5\%$  and a  $Re$  of 5000 for an attack angle of a)  $30^\circ$ , b)  $45^\circ$ , and c)  $60^\circ$



**Figure 6**

The NF velocity distribution at  $\phi = 1.5^\circ$  and  $Re = 5000$  for an attack angle of a)  $30^\circ$ , b)  $45^\circ$ , and c)  $60^\circ$

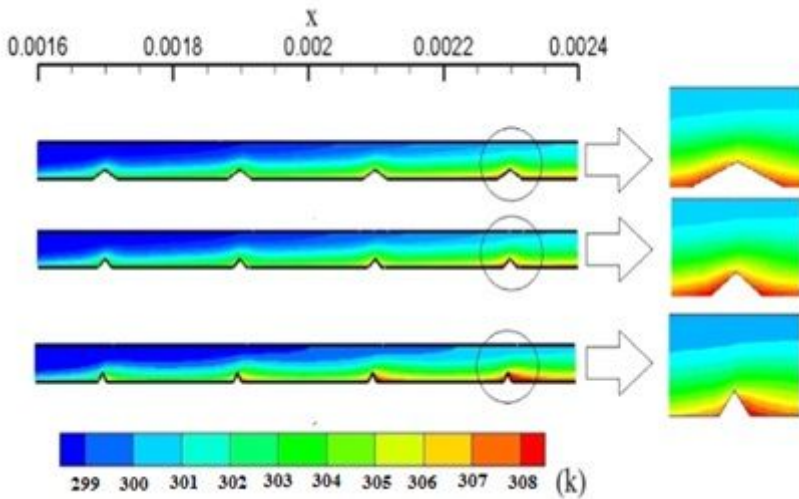


**Figure 7**

The temperature distribution for the NF at  $\phi = 1.5^\circ$  and  $Re = 5000$  for an attack angle of a)  $30^\circ$ , b)  $45^\circ$ , and c)  $60^\circ$

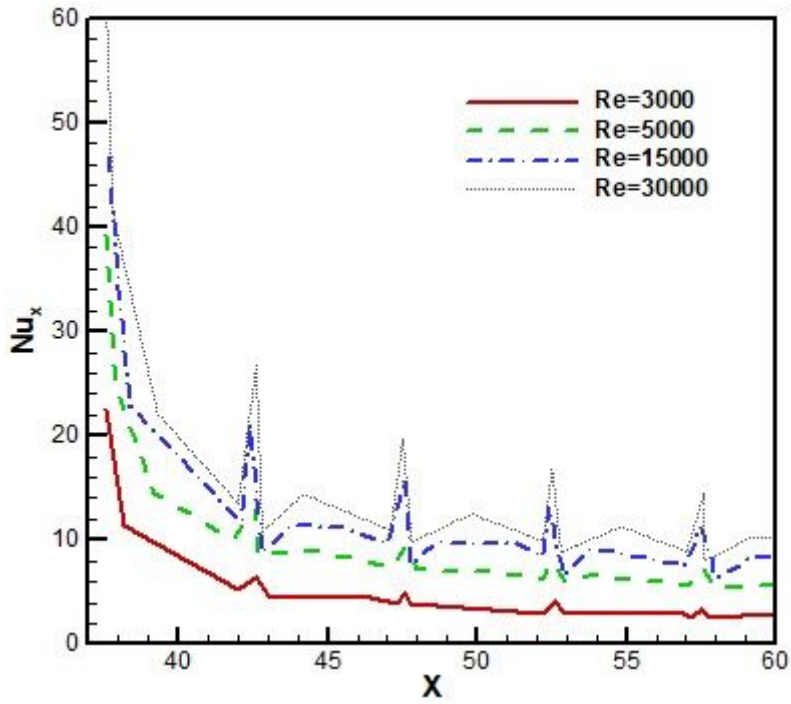


Figure 8

$Nu$  variations in the triangular vortex generator channel direction at an attack angle of  $30^\circ$ ,  $\phi=0.5\%$ , a vortex generator height of 3 mm, and different  $Re$

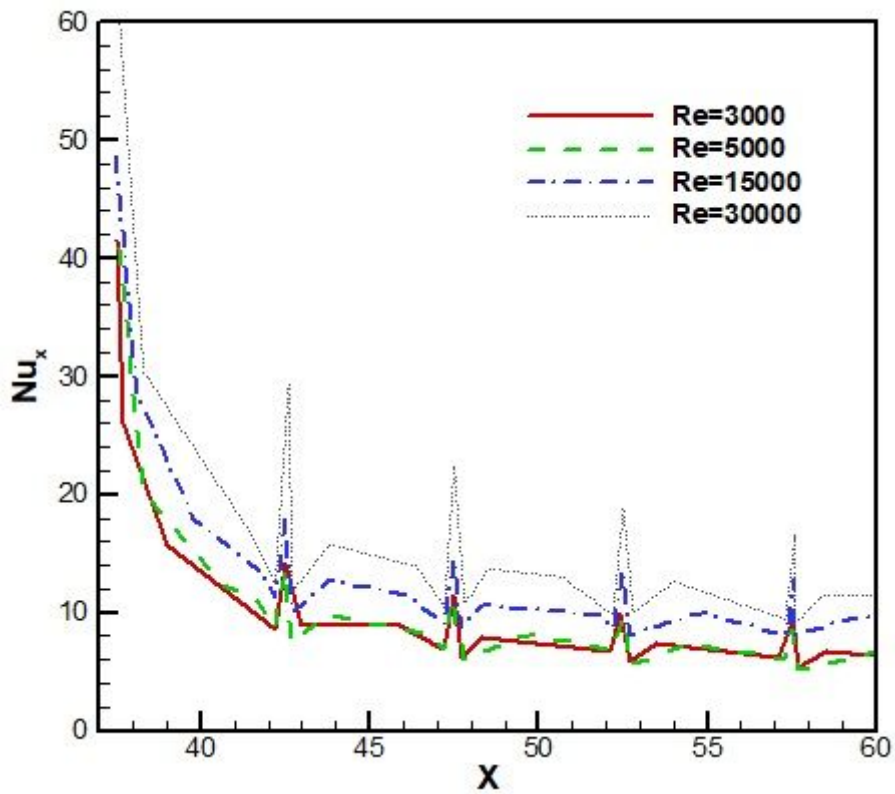


Figure 9

Local Nu variations in the triangular vortex generator channel direction at an attack angle of  $45^\circ$ ,  $\varphi=0.5\%$ , a vortex height of 3 mm, and different Re

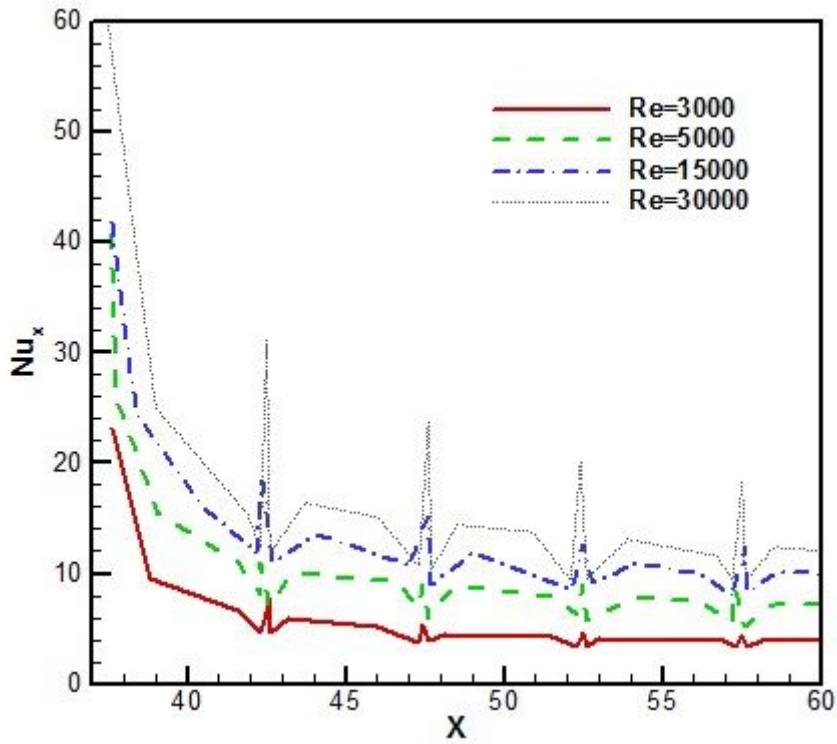


Figure 10

Nu variations in the triangular vortex generator channel direction at an attack angle of  $60^\circ$ ,  $\varphi=0.5\%$ , a vortex height of 3 mm, and different Re

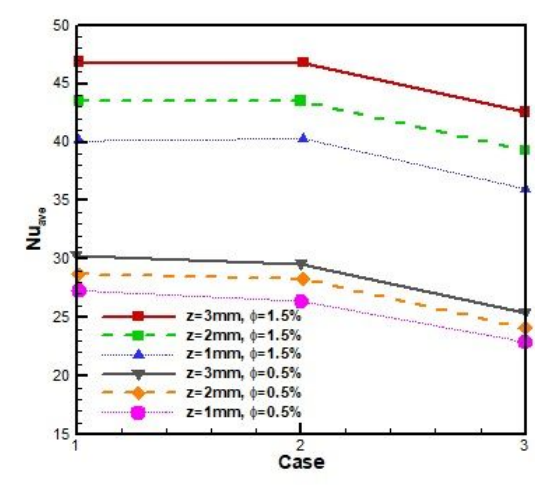
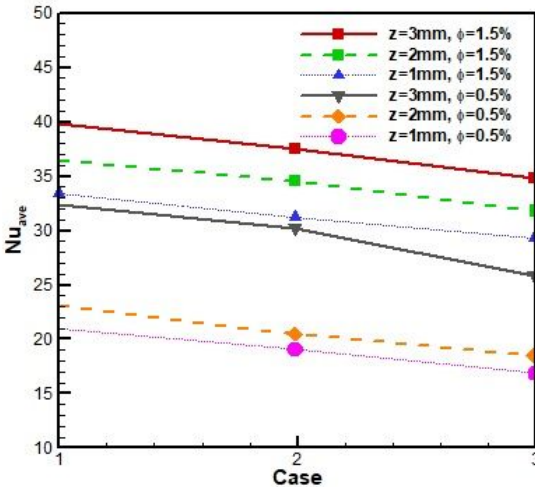
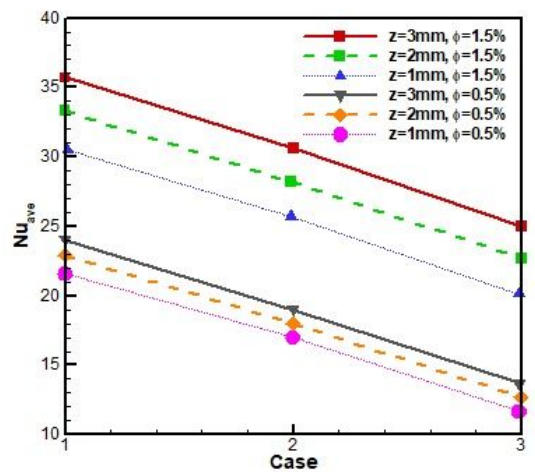


Figure 11

Nu variations for different cases of the triangular vortex generator channel at different volume fractions and the Re of a) 5000, b) 15000, and c) 30000

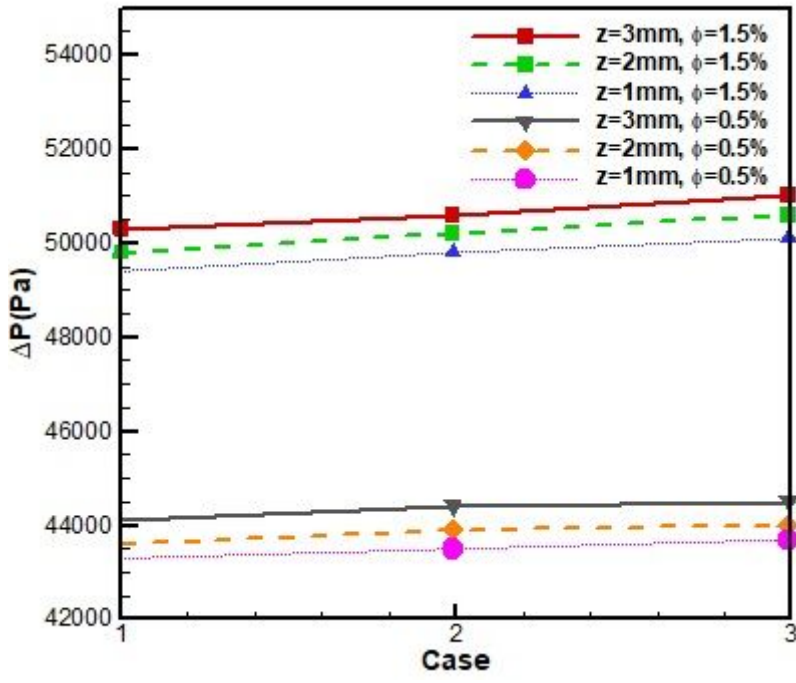


Figure 12

Pressure drop variations at a Re of 3000 and different vortex generator attack angles, volume fractions, and vortex generator depths